

Time-Dependence of the Mass Accretion Rate in Cluster Cooling Flows

Eric A. Lufkin^{1,2,3}, Craig L. Sarazin¹ and Raymond E. White III^{2,3}

ABSTRACT

We analyze two time-dependent cluster cooling flow models in spherical symmetry. The first assumes that the intracluster gas resides in a static external potential, and includes the effects of optically thin radiative cooling and mass deposition. This corresponds to previous steady-state cooling flow models calculated by White & Sarazin (1987). Detailed agreement is found between steady-state models and time-dependent models at fixed times in the simulations. The mass accretion rate \dot{M} is found either to increase or remain nearly constant once flows reach a steady state. The time rate of change of \dot{M} is strongly sensitive to the value of the mass deposition parameter q , but only mildly sensitive to the ratio β of gravitational binding energy to gas temperature. We show that previous scaling arguments presented by Bertschinger (1988) and White (1988) are valid only for mature cooling flows with weak mass deposition ($q \lesssim 1$). The second set of models includes the effects of a secularly deepening cluster potential and secondary infall of gas from the Hubble flow. We find that such heating effects do not prevent the flows from reaching a steady state within an initial central cooling time.

Subject headings: cooling flows — galaxies: clusters: general — hydrodynamics — intergalactic medium — X-rays: general

1. Introduction

X-ray and optical data strongly suggest that cooling accretion is taking place in more than half of galaxy clusters (for a review, see Fabian 1994). In non-cooling flow clusters, X-ray surface brightness profiles obtained from imaging data are usually well modeled by a single-temperature gas in hydrostatic equilibrium with a background isothermal potential (Jones & Forman 1984). In contrast, cooling flow clusters exhibit significant excess central emission compared to that derived

¹Department of Astronomy, University of Virginia, PO Box 3818, Charlottesville, VA 22903-0818

²Department of Physics & Astronomy, University of Alabama, Box 870324, Tuscaloosa, AL 35487-0324

³Code 662, NASA Goddard Space Flight Center, Greenbelt, MD 20771

from a fit to an isothermal. This excess emission is thought to be due to gas losing its thermal energy and condensing out of the intracluster medium (ICM) at rates that often exceed $100 M_{\odot} \text{ yr}^{-1}$. Over a cluster lifetime, the central dominant galaxies in these clusters may accrete up to $\sim 10^{12} M_{\odot}$ of cooled gas. (We assume a Hubble constant of $50 \text{ km s}^{-1} \text{ Mpc}^{-1}$ and that a cluster lifetime is comparable to a Hubble time.)

X-ray surface brightness profiles of cooling flow clusters can be used to infer mass accretion rates \dot{M}_{surf} which increase roughly linearly with radius from the centers of cooling flows (e.g., Stewart et al. 1984; Thomas, Fabian, & Nulsen 1987). If the flows are steady, this in turn implies that matter must be cooling and condensing out of the ICM over the full range of radii ($\gtrsim 100 \text{ kpc}$) for which cooling flow emission is observed. If there were no distributed mass deposition, then gas would be deposited only at the center. The resulting X-ray surface brightness profiles would be significantly more centrally peaked than those observed.

X-ray spectra of cooling flows imply cooling rates \dot{M}_{spec} within a factor of two of those inferred from the imaging data (e.g., Canizares, Markert, & Donahue 1988; Allen et al. 2000). This result is an independent confirmation of the accretion rates derived from imaging data. The dynamical accretion rate in a spherical system, $\dot{M} = 4\pi r^2 \rho u$ (where ρ is the gas density and u is the flow velocity), is not observed directly. Although the dynamical and X-ray-derived accretion rates should be the same if the flow is in a steady state, the radial velocities in the accretion flow are typically on the order of tens of kilometers per second, well below both the velocity dispersion of a single galaxy and the spectral resolution of current X-ray instruments.

Although the final repository for the cooling gas remains ambiguous, the evidence is quite strong that it is cooling and decoupling from the flow (Fabian 1994; White, Jones, & Forman 1997; Peres et al. 1998; Markevitch et al. 1998; Allen et al. 2000; White 2000). Heating processes are unlikely to balance cooling since their functional dependences on density and temperature do not match those for radiative losses. Indeed, previous numerical investigations have shown that alternatives to large cooling accretion rates, such as heat conduction (Bregman & David 1988; Meiksin 1988), supernova heating, and drag heating by orbiting galaxies (Bregman & David 1989), are able to reproduce the data only for narrow ranges in the respective free parameters, if at all. Moreover, it is difficult to imagine a process other than cooling that can power an excess emission rate as high as $10^{44} \text{ erg s}^{-1}$ without producing other noticeable signatures. Finally, most alternatives to cooling accretion fail to account for observed soft X-ray lines.

Models that assume a steady accretion flow with mass deposition can reproduce the observed X-ray features of cluster cooling flows (e.g., White & Sarazin 1987, hereafter WS; Fabian 1994). WS calculated steady-state models with a simple mass deposition formation law, but such models provide no information on the evolution of cooling flows.

In this paper we use a suite of time-dependent spherical models to assess the evolution of cooling flows in static and evolving gravitational potentials. In addition to providing predictions of the spatial structure and spectral properties of relatively relaxed cluster cooling flows, the spherical

model also has implications for their long term evolution. The time evolution of the accretion rate has consequences for the total amount of accreted material in cooling flows, and it can provide a test for the models when compared to X-ray observations of high-redshift clusters. Two free parameters likely to affect the time-variation of \dot{M} in the spherical models are the mass deposition efficiency and the ratio β of gravitational binding energy to thermal energy in the gas. The parameter β determines the shape of the gas distribution in clusters when the gas is in hydrostatic equilibrium.

Self-similar models can offer insight into the evolutionary effects, and they provide a useful testing ground for fully time-dependent calculations (Chevalier 1987, 1988; Bertschinger 1989; Lufkin & Hawley 1993). However, they are limited in that they allow either a narrow range of initial conditions or a limited number of physical processes. As a result, such models have not been successful in attaining detailed agreement with the observations. Simple scaling arguments are potentially useful (Bertschinger 1988; White 1988), and we review these in § 2 below. Our numerical simulations of cooling flow evolution in static gravitational potentials are presented in § 3.

As a final point of inquiry, we examine the consequences of continued cluster evolution by investigating the effects of a secularly deepening cluster potential and continued accretion of gas from the Hubble flow. We present a simple physical argument in § 2.3 which shows that adiabatic compression of gas in a deepening gravitational potential does not inhibit cooling flows. Our numerical simulations of cooling flow evolution in an evolving gravitational potential are described in § 4 and compared to similar work by Meiksin (1990, hereafter M90). Our conclusions differ from those in M90, which found that cooling flows are slow to reach steady state and mass dropout rates were strongly reduced by time-dependent effects in an evolving gravitational potential. We do not find these effects in our simulations of cooling flows evolving in the same deepening gravitational potential as used in M90, which is consistent with the simple arguments we present in § 2.3. Our results are summarized in § 5.

2. Physical Arguments

Before proceeding to the numerical models, we first discuss some physical arguments regarding the temporal behavior of cooling flow clusters. These include definitions of the various physical regions in the flow, a review of analytic predictions of the time dependence of the cooling accretion rate \dot{M} , and a discussion of whether adiabatic compression can extend the cooling time. These physical arguments form a basis for the discussion of the numerical models.

The most important process in models for cooling flows is obviously the radiative cooling of the gas. Over essentially all of the region of the flow, this occurs on a timescale which is much longer than the dynamical time of the gas, and as a result the flows and compression which occur are relatively slow. We do not include thermal conduction or other diffusive processes in our calculations. The only other processes which affect the temperature of the gas are shocks and

adiabatic compression or expansion of the gas. In the absence of cluster mergers, the flow velocities are low and shocks are not important in our models. However, adiabatic compression of the gas will occur as a result of the cooling and inflow of the gas in the gravitational potential, or through the slow cosmological growth in the cluster potential. We discuss the effects of adiabatic heating on the cooling time scale of the gas in § 2.3 below.

2.1. Timescales

The general structure of cluster cooling flows in a static potential is determined by three characteristic timescales: the age of the cluster t_{age} , the cooling time t_{cool} and the dynamical time t_{dyn} . The instantaneous isobaric cooling time is

$$t_{\text{cool}} = \frac{5}{2} \frac{kT}{\mu m_p \rho \Lambda(T)} \approx 5 \times 10^9 \left(\frac{T}{10^8 \text{ K}} \right) \left(\frac{\Lambda}{5 \times 10^{24} \text{ ergs cm}^3 \text{ s}^{-1} \text{ g}^{-2}} \right)^{-1} \left(\frac{n}{10^{-2} \text{ cm}^{-3}} \right)^{-1} \text{ yr}, \quad (1)$$

where μ is the mean molecular weight in units of the proton mass m_p (we assume $\mu = 0.6$ in this work), and $n = \rho/\mu m_p$ is the total particle number density. The function $\Lambda(T)$ is the cooling rate such that $\rho^2 \Lambda$ has the units $\text{erg s}^{-1} \text{ cm}^{-3}$. We assume the cooling function of WS for half-solar abundances. The dynamical time is

$$t_{\text{dyn}} \approx 10^8 \left(\frac{\sigma_c}{1000 \text{ km s}^{-1}} \right)^{-1} \left(\frac{r_c}{100 \text{ kpc}} \right) \text{ yr}, \quad (2)$$

where r_c is the cluster core radius and σ_c is the velocity dispersion of the cluster galaxies (also nearly equal to the initial sound speed in the gas prior to cooling).

The cooling radius r_{cool} is defined as the point where the instantaneous isobaric cooling time equals the system age. Inside the cooling radius, the cooling time is less than the age of the system, and a cooling flow occurs. As long as the cooling time exceeds the dynamical time, the gas flows subsonically into the center, regulated by cooling. If the gas cools completely before reaching the center and the rate of mass drop out is not too large ($q \lesssim 3$), the flow generally passes through a sonic radius r_s , where the flow speed equals the local sound speed (Sarazin & Graney 1991). For $r_{\text{cool}} \gg r \gg r_s$ the system is expected to be reasonably well-described as being in steady-state, an assumption which we test explicitly in § 3.3. The validity of the steady-state approximation at $\sim r_{\text{cool}}$ cannot be assessed except with time dependent models.

The above definition for the cooling radius is straightforward, as well as familiar, but it may not be the most useful. Since the gas is flowing inward as it cools, we consider whether a more relevant timescale may be the *integrated* isobaric cooling time

$$t_{\text{int}} = \frac{5}{2P} \int_0^\theta \frac{\theta' d\theta'}{\Lambda(\theta')}, \quad (3)$$

where $\theta \equiv kT/\mu m_p$. Typically, the integrated cooling time t_{int} is about a factor of two shorter than the instantaneous cooling time t_{cool} . Consequently, gas may actually be taking part in the flow out to a considerably larger radius r_{int} , where $t_{\text{int}} = t_{\text{age}}$. We comment more on this in § 3.2.

2.2. \dot{M} as a Function of Time

The time-dependent calculations of §§ 3 and 4 solve explicitly for the accretion rate \dot{M} as a function of time. However, it may also be possible to estimate $\dot{M}(t)$ based on the assumption that gas outside the cooling radius remains unaffected by cooling in the interior. Writing the dynamical accretion rate as $\dot{M} = 4\pi r^2 \rho u$, one might expect that the velocity can be approximated by the propagation rate of the cooling radius, so that \dot{M} is interpreted as the rate at which gas is swept over by the cooling radius. This amounts to making the substitution $u = dr_{\text{cool}}/dt|_{t_{\text{cool}}}$. With this approximation, White (1988) showed that the cooling radius evolves with time as $r_{\text{cool}} \propto t^\eta$, where $\eta = [(1 - \Delta_T \Lambda) \Delta_r T - \Delta_r \rho]^{-1}$, and where we have used the notation $\Delta_x \equiv (d \ln / d \ln x)$. The exponent of the time dependence in the accretion rate \dot{M} is then given by

$$\Delta_t \dot{M} = (3 + \Delta_r \rho) \eta - 1 \equiv \xi. \quad (4)$$

If the gas is initially isothermal, then $\xi < (>) 0$ when $\Delta_r \rho < (>) -3/2$. In other words, cooling flow accretion rates will increase (decrease) with time when the cooling radius is in a region where the gas density profile is shallower (steeper) than $r^{-1.5}$.

The gas density profiles of clusters of galaxies are often fit with the isothermal “beta” model. In this model, the gas density distribution is given by

$$\rho(r) = \rho_0 \left[1 + \left(\frac{r}{r_c} \right)^2 \right]^{-3\beta/2}, \quad (5)$$

where ρ_0 is the central gas density (e.g., Jones & Forman 1984). We will sometimes give $n_0 \equiv \rho_0/\mu m_p$, which is the corresponding total particle number density. If the galaxies in a cluster are isothermal with a distribution given by the analytic King approximation to an isothermal sphere, then β is determined by the ratio of the velocity dispersion of the galaxies to that of the gas,

$$\beta = \frac{\mu m_p \sigma_c^2}{kT}. \quad (6)$$

Typically, clusters have $\beta \approx 2/3$, and the density profile tends to steepen from $\Delta_r \rho \approx 0$ near the center to $\Delta_r \rho \approx -2$ at large radii. Thus, there will be a transition radius r_{tran} where $\xi \equiv \Delta_t \dot{M}$ changes sign from positive to negative. For cases where $r_{\text{cool}} > r_{\text{tran}}$, one would infer from equation (4) that \dot{M} is decreasing. However, there appears to be some variation in the value of β from cluster to cluster, from 0.5 to about 1.2. This variation translates into a variation in the gas scale height relative to cluster core radii, and hence in the value of ξ at the cooling radius. There is a correlation between cluster temperatures (both the gas temperatures at large radii and the

dynamical temperatures [velocity dispersions] of galaxies in clusters) and the overall slope of the X-ray surface brightness profiles (White 1991), implying that hot clusters ($T_{\text{gas}} \gtrsim 7 \times 10^7$ K) tend to have density profiles scaling as $\rho \sim r^{-2}$ at large radii, while cool clusters ($T_{\text{gas}} \lesssim 5 \times 10^7$ K) have shallower profiles. There is therefore a range of cases, with both increasing and decreasing mass accretion rates inferred via equation (4). In cases where imaging data imply a cooling flow, the slope of the X-ray surface brightness profile typically does not make a sudden inflection at either a core or cooling radius. Consequently, determining the transition radius from imaging alone is particularly difficult. Thus, in the absence of spatially resolved spectroscopy, there is some *a priori* ambiguity in the sign and magnitude of $d\dot{M}/dt$. In § 3, we investigate this question for a plausible range in β .

2.3. Adiabatic Compression

One obvious limitation to the analysis of § 2.2 is its failure to account for ongoing dynamical evolution of the cluster itself. As subclusters merge, and as matter continues to accrete from the Hubble flow, the cooling flow may be altered, or disrupted altogether. A 1-D calculation can take these processes into account only in the limit of quasi-static deepening of the cluster potential well. Observations (Bird 1994) and numerical simulations (Evrard 1990) of hierarchical structure formation show that the growth of galaxy clusters is only roughly approximated by a spherically symmetric deepening of a cluster’s gravitational potential. If the changes in the cluster potential result from violent subcluster mergers, shocks may be driven into the gas. Such mergers cannot be easily modeled in a 1-D simulation. Nonetheless, following work by M90, we consider a simple model in which the growth of the cluster is described by a slow deepening of the cluster potential and the resulting adiabatic compression of the intracluster gas. Although this is a simplistic approximation, we can still address the question of whether such adiabatic compression is sufficient to change the qualitative nature of the steady flow compared to that of an isolated, static cluster, as has been suggested by M90.

A simple physical argument shows that adiabatic compressive heating is not sufficient to balance radiative cooling in intracluster gas. The point is that, whatever the cause of such compression, it is a reversible process and consequently does not change the entropy of the gas. Thus, the only changes in the entropy are those due to radiative cooling. Consider a parcel of gas initially at temperature T_i and density ρ_i , with an adiabatic index γ . For the purpose of this argument, we approximate the cooling function as a power law, $\Lambda \propto T^\alpha$. Adiabatic compression to density ρ_f will heat the gas to a temperature of $T_f = T_i(\rho_f/\rho_i)^{\gamma-1}$. The cooling time scales as $T^{1-\alpha}\rho^{-1}$, so, after compression, the cooling time is

$$t_{\text{cool},f} = t_{\text{cool},i} \left(\frac{\rho_f}{\rho_i} \right)^{\gamma+\alpha-\gamma\alpha-2}. \quad (7)$$

For $\gamma = 5/3$ the effect of compressional heating is exactly balanced by the increased cooling rate for a critical value $\alpha = \alpha^* = -1/2$. We note that $\alpha \gtrsim -1/2$ for almost all temperatures in the range

$10^6 \leq T \leq 10^9$, except for a narrow range between $T \approx 10^7$ K and $T \approx 3 \times 10^7$ K (e.g., Raymond, Cox, & Smith 1976; WS). Thus, adiabatic compression generally should *decrease* the cooling time for a given parcel of gas. This result is independent of the physical processes responsible for the compression.

3. Time-Dependent Flow in a Static External Potential

3.1. Assumptions and Equations

The models in this section are designed to resemble those of WS for the purpose of assessing time-dependent effects in existing models with mass deposition. We therefore include radiative cooling and a mass deposition term, but ignore the effects of conduction and external heating, referring discussion of the latter to the published literature. Neglecting angular momentum, the corresponding spherically symmetric fluid equations are

$$\frac{d\rho}{dt} + \frac{\rho}{r^2} \frac{\partial}{\partial r}(r^2 u) = -\dot{\rho} \quad (8)$$

$$\frac{du}{dt} + \frac{1}{\rho} \frac{\partial P}{\partial r} + \frac{\partial \Phi}{\partial r} = 0 \quad (9)$$

$$P \frac{d}{dt} \ln(P \rho^{-\gamma}) = -(\gamma - 1) \rho^2 \Lambda(T), \quad (10)$$

where P and T are the pressure and temperature respectively, $\rho^2 \Lambda$ is the cooling rate in $\text{erg s}^{-1} \text{cm}^{-3}$, Φ is the total gravitational potential and

$$\frac{d}{dt} \equiv \frac{\partial}{\partial t} + u \frac{\partial}{\partial r}.$$

For the mass dropout rate $\dot{\rho}$ we adopt the cooling-time law of WS,

$$\dot{\rho} = q \frac{\rho}{t_{\text{cool}}}, \quad (11)$$

where q is an efficiency factor of order unity and t_{cool} is defined in equation (1). This mass deposition law is based on the *ansatz* that thermal instabilities due to cooling lead to growing perturbations which leave the flow over a range of radii. (It is often expedient in numerical simulations to cut off the cooling function at some floor temperature T_{floor} , the value of which is arbitrary provided that the gas temperature does not reach T_{floor} unless the flow becomes supersonic.)

We solve equations (8)–(10) using a time-explicit hydrodynamics code in spherical symmetry (Lufkin & Hawley 1993). The code is similar to existing second-order Eulerian codes except that it solves the fluid equations in Lagrangian mode with a globally conservative remap to the fixed grid. The code has been tested on a variety of problems, including self-similar cooling flows and cosmological accretion (for details, see Lufkin & Hawley 1993).

3.1.1. The Assumed Mass Deposition Efficiency q

All of the cooling flow models considered here have a finite mass deposition efficiency coefficient q . If one assumes no mass deposition, the mass accretion rate is constant with radius in a steady-state flow, and the gas cools catastrophically at the center (WS; Meiksin 1988, 1990), i.e., the cooling is sufficiently strong for the gas to pass through a sonic point as it approaches the center. The catastrophe is prevented (i.e. the flow remains subsonic all the way to the center) for $q \gtrsim 3.4$. The dynamical mass accretion rate \dot{M} is also found to be roughly proportional to radius for $q \approx 3 - 4$. Although a smaller q cannot be ruled out observationally in all cases, a value as small as $q = 0$ implies an X-ray surface brightness profile that is much too sharply peaked in the center. We therefore restrict our attention to the two cases $q = 1$ (below which the central density is too sharply peaked) and $q = 4$, and examine the effect of this variation on model flows.

For these applications, the numerical grid covers the full dynamic range from scales of ~ 1 kpc near the center out to a radius of several Mpc, with a reflecting inner boundary ($u \rightarrow 0$ as $r \rightarrow 0$). In the $q = 1$ case there is generally a sonic radius near $r \sim 1$ kpc in the steady-state models. The sonic radius is therefore unresolved by the grid spacing of ~ 1 kpc near the center in the time-dependent models. If an outflow boundary inner condition is used, the grid must resolve the region between the sonic radius and the origin, in order to have supersonic outflow at the inner grid boundary (Lufkin & Hawley 1993). Unfortunately, timestep constraints prevent the use of an outflow boundary in this case, owing to gas velocities in excess of 100 km s^{-1} inward from the sonic radius.

3.1.2. The Background Cluster

The initial conditions for the time-dependent simulations are chosen such that the gas is isothermal and in hydrostatic equilibrium with the external potential Φ . Integrating the hydrostatic equation we obtain for the initial density profile

$$\rho(r)_{t=0} = \rho_0 \exp \left\{ -[\Phi(r) - \Phi_0]/(kT_\infty/\mu m_p) \right\}, \quad (12)$$

where T_∞ is the asymptotic gas temperature at large radii, and ρ_0 and Φ_0 are the density and potential at $r = 0$. The background potential for the cluster gas is assumed be that of a massive central galaxy Φ_g plus a smooth cluster component Φ_c . The cluster mass distribution is taken as a King approximation to an isothermal sphere:

$$\rho_c(r) = \rho_{c0} \left[1 + (r/r_c)^2 \right]^{-3/2}, \quad (13)$$

where r_c is the cluster core radius. The potential for this distribution is given by

$$\Phi_c(r) = -\Phi_{c0} \frac{\ln \left[r/r_c + \sqrt{1 + (r/r_c)^2} \right]}{r/r_c}. \quad (14)$$

The central potential $\Phi_{c0} = 4\pi G\rho_{c0}r_c^2$ and is related to the line-of-sight velocity dispersion σ_c by $\Phi_{c0} = 9\sigma_c^2$. We assume $\sigma_c = 1054 \text{ km s}^{-1}$ ($\Phi_{c0} = 10^{17} \text{ erg g}^{-1}$) for the hot cluster runs, and $\sigma_c = 527 \text{ km s}^{-1}$ for the cool cluster runs. The corresponding cluster masses inside of 250 kpc are 10^{14} and $5 \times 10^{13} M_\odot$, respectively.

We note that our adopted potential has a finite depth, whereas a true isothermal is infinitely deep. Consequently, the density profile for the gas becomes sufficiently shallow at large radii that the total X-ray luminosity diverges. This actually follows from assuming that the gas at large radii is hydrostatic and isothermal, which cannot be true on spatial scales where the sound crossing time is greater than a Hubble time ($r \sim 10 \text{ Mpc}$). In the evolving cluster models of § 4, the outer parts of the cluster are in free fall from the cold Hubble flow, with an accretion shock at a radius of 3–10 Mpc. Because the cooling flow is confined to the inner 100 kpc or so, the solution is not sensitive to the structure of the cluster much beyond this radius. We therefore quote total luminosities within one half and two Mpc. Furthermore, because gas densities far from the center are not well constrained observationally, we omit discussion of the structure of the ICM at very large radii.

3.1.3. The Central Galaxy

All of the models here and below assume the presence of a massive, stationary central galaxy. However, in choosing a form for the galactic potential we are guided by the desire to extend these models to higher dimensions, with the possibility of allowing a galaxy to orbit in the cluster (e.g., Lufkin, Balbus, & Hawley 1995). The primary considerations are computational efficiency and accuracy when the galaxy’s position changes with time. The potential should be smooth and fully resolved, with $\nabla\Phi_g \rightarrow 0$ as $r \rightarrow 0$ to avoid grid noise. It should also be expressible in terms of simple analytic functions. A potential of the form of equation (14) would be one possibility. However, the mass in this model diverges logarithmically, and it is generally preferable to have a galaxy potential corresponding to a finite mass. While it is tempting to truncate an analytic King model at some finite radius, this can generate anomalous sound waves for an orbiting galaxy on a finite difference grid.

A simple form which satisfies our numerical criteria is Plummer’s model (Binney & Tremaine 1987):

$$\Phi_g = \Phi_{g0} \left(1 + r^2/r_g^2\right)^{-1/2}, \quad (15)$$

where r_g is a characteristic radius. As it stands, the density distribution which gives rise to equation (15) does not approximate real galaxies well. However, we have found that a superposition of suitably weighted components can give a good approximation to a King model. For example, the addition of two potentials, one for the center and one for an extended distribution, can be written as

$$\Phi_g = \Phi_{g0} \left[\frac{(1-y)}{(1+r^2/r_g^2)^{1/2}} + \frac{y}{(1+r^2/r_t^2)^{1/2}} \right], \quad (16)$$

where $0 < y < 1$ and r_t is the characteristic radius of the extended component. We have chosen to specify the potential directly, rather than starting from the underlying density distribution. This is because the gas interacts with the galaxy only through gradients in the potential. The analytic form we have chosen contains functions which can be calculated at high speed, whereas transcendental functions (such as power laws, logarithms and arctangents) can increase the run time significantly. The square root function is an exception. It uses a divide-and-average algorithm, which converges very fast. A tabulated function, although not particularly expensive, can be rather unwieldy, especially when a galaxy’s position changes with time.

At large radii, ($r \gg r_t$), the potential tends to that of a point mass, so that the total mass has the finite value

$$M_g = \frac{[(1-y)r_g + yr_t]\Phi_{g0}}{G}. \quad (17)$$

For $y = 0.15$ and $r_t^2 = 40r_g^2$, the gradient of this potential closely approximates that of an analytic King model truncated at $r = 20r_g$.

We note that in equations (13) and (14), r_c is a true core radius (i.e., it corresponds to the radius at which the surface density falls to one half of its central value). In the model galaxy chosen here, this occurs at a radius of about $0.63r_g$. Figure 1 shows $g = -\partial\Phi_g/\partial r$ for a King model in which the central potential is $\Phi_{g0} = 7\sigma_g^2$ (solid line; see Binney & Tremaine 1987), compared with truncated (short dash) and nontruncated (dotted) King approximations to an isothermal sphere. These are plotted along with a model galaxy with a potential of the form of equation (16), for $y = 0.15$, $r_g = 1.58r_c$, $r_t = 10r_c$ (long dash). The vertical scale is in arbitrary units, and can be set either by the central potential or the total mass of the galaxy M_g .

In the simulations below, the core radii r_c are 250 kpc for the cluster and 4.41 kpc for the central galaxy ($r_g = 7$ kpc). Assuming a total mass for the galaxy of $2 \times 10^{12} M_\odot$ implies a line-of-sight velocity dispersion of 288 km s^{-1} at the center and 251 km s^{-1} averaged over a circular aperture subtending a radius of 10 kpc, in the manner of Bailey & MacDonald (1981). The composite density distribution can also be reasonably approximated by an NFW profile (Navarro, Frenk, & White 1997) with a scaling radius of $r_s \sim 200$ kpc.

3.2. Results

Table 1 lists the input parameters and some of the calculated global characteristics for ten simulations. Each of five model clusters are evolved for 15 Gyr for $q = 1$ and $q = 4$. The first model, (runs 1 and 2) is taken to be typical of a strong cooling flow in a hot cluster, and is discussed in detail in §§ 3.2.1. The second model (runs 3 and 4) corresponds to a relatively cool cluster and is discussed in § 3.2.2. The remaining three cluster models, also discussed in § 3.2.2, are used to explore a range of values in β . The results of runs 1–4 are plotted in Figures 2 – 9, and are compared to steady-state calculations in § 3.2.3.

The physical assumptions, as stated above, are identical to those in WS, with the exception of the form of the external potential. Self-gravity is neglected for the static models, but is included in the evolving cluster models in § 4 below. Because the cooling flow is primarily pressure-driven, the inclusion of self-gravity has little effect.

3.2.1. Hot Cluster Runs

Shown in Figure 2 are the density, temperature, mass accretion rate and cooling times as functions of radius at various times in the evolution, for the hot cluster run with $q = 1$. The initial conditions, given in Table 1, are chosen so that the models have reasonable global properties at $t = 10^{10}$ yr in the evolution. In discussing the properties of the models, we use an age of 10^{10} yr as a fiducial time for comparison to observed clusters. The solid curves in the figures refer to this fiducial age. More generally, the dotted, short-dashed, long-dashed, solid and dot-dashed lines correspond to ages of 0, 3, 6, 10 and 15 Gyr, respectively. The curve at 15 Gyr (beyond the fiducial age) is included to show that a steady state has been reached.

Figure 3 shows the time evolution of both the instantaneous and integrated cooling radii, r_{cool} and r_{int} . We also give the dynamical mass accretion rate $\dot{M} = -4\pi r^2 \rho u$ as determined at each of these cooling radii. The X-ray-derived mass accretion rate (or cooling rate) \dot{M}_X is determined by assuming that all of the X-ray luminosity from within the cooling radius is due to gas cooling within that radius. This is the standard assumption made in analyses of the X-ray surface brightness profiles to derive the total cooling or accretion rates \dot{M}_{surf} (e.g., Thomas et al. 1987). (Recall that $\dot{M}_X = \dot{M}$ only for steady state flows.) As expected, there is close agreement between \dot{M} and \dot{M}_X at each radius, although the value of \dot{M} at r_{int} is nearly twice that at r_{cool} . The panel at lower right shows the value of $\xi \equiv \Delta_t \dot{M}$ as derived from local gradients in the simulation (eq. 4). We find $\xi \approx 0.29$ at r_{int} and $\xi \approx 0.59$ at r_{cool} . The value at r_{cool} compares reasonably to a value of $\Delta_t \dot{M} \approx 0.34$ measured directly from the simulation by least-squares fitting of a straight line to $\log \dot{M}(t)$ as measured at r_{cool} and dumped every 10^8 years.

We determine the transition radius (where $\xi = 0$ in eq. [4]) by examining the numerical results directly: $r_{\text{tran}} = 234$ kpc at $t = 10^{10}$ yr. The measured cooling radius at this time is $r_{\text{cool}} = 100$ kpc $< r_{\text{tran}}$, so we would infer from equation (4) that the accretion rate is increasing, as Figure 3 confirms. There are several sources of error in the estimate of r_{cool} . The grid spacing is about 5 kpc in this region, although this can be reduced if necessary by running the problem at higher resolution. More serious is the assumption that the relevant characteristic radius is r_{cool} , not r_{int} (see eqs. 1 and 3). At $t = 10^{10}$ yr in the $q = 1$ case, the location where $t_{\text{int}} = t_{\text{age}}$ is $r_{\text{int}} = 151$ kpc $< r_{\text{tran}}$. Thus we see that the scaling relation of § 2.2 is confirmed in this case for both measures of the cooling radius.

Several other features are noticeable from the figures. Gas in the core has cooled completely between 6 and 10 Gyr, with little change in the flow thereafter. The initial cooling time at the center

is 10.8 Gyr, but the integrated isobaric cooling time is 6.43 Gyr. This time period corresponds to the phase in which the cooling radius and mass accretion rates slow to a steady rate of increase (Figure 3). The particular shape of the temperature profile is determined by the cooling function and the shape of the potential, while the density and accretion rate profiles are nearly featureless. Because the sonic radius is unresolved, the innermost grid zones reflect low-amplitude sound waves into the flow. These are visible in the accretion rate at 15 Gyr, but do not significantly affect the flow.

One might expect an inflection point in the density profile as the center begins to cool, but this is not observed. The entire inner region cools almost simultaneously, but isobarically, resulting in a smooth transition to the steeper density profile seen at later times.

The hot cluster $q = 4$ solution (run 2) is shown in Figures 4 and 5. This model has a higher rate of mass drop out at larger radii. In this case, the initial density required to recover an accretion rate of about $300 M_{\odot} \text{ yr}^{-1}$ at $t = 10$ Gyr is sufficiently high ($n_0 = 0.033 \text{ cm}^{-3}$) that the center cools in about 5 Gyr. After this time we find that \dot{M} is slowly decreasing, even though both cooling radii ($r_{\text{cool}} = 74 \text{ kpc}$; $r_{\text{int}} = 128 \text{ kpc}$) lie well inside $r_{\text{tran}} = 354 \text{ kpc}$. Moreover, the logarithmic rates of change of \dot{M}_X measured at both r_{int} and r_{cool} are approximately equal $\xi \approx -0.45$, whereas the value predicted by equation (4) goes no lower than $\xi = -0.2$ for this time frame. The value of $\eta \equiv d \ln r_{\text{cool}} / d \ln t$ is also discordant; we measure $\eta \approx 0.5$ from the simulations, whereas the density and temperature profiles would suggest a value of $\eta \approx 1.0$. Thus, it appears that the scaling argument detailed in § 2.2, which assumes $q = 0$, breaks down for large values of q . We will comment more on this below. Because there is no sonic point in this model, there is no need for high resolution in the innermost regions of the flow.

3.2.2. Cool Cluster Runs

We perform a second pair of simulations in which all the input parameters are the same as those above except that the cluster has a central velocity dispersion of $\sigma_c = 527 \text{ km s}^{-1}$ and the asymptotic gas temperature is $T_{\infty} = 3 \times 10^7 \text{ K}$. These parameters imply $\beta = 0.6$ (run 3 and 4 in Table 1), compared with $\beta = 0.75$ in the hot cluster simulations. The results for runs with $q = 1$ and $q = 4$ are shown in Figures 6–9. The same general comments regarding the hot cluster models also apply in this case. The $q = 1$ case shows an accretion rate \dot{M} that is increasing with time, in agreement with the arguments in § 2.2, while the $q = 4$ case shows a nearly constant \dot{M} even though the predicted ξ is clearly positive near the cooling radius and nowhere negative.

There is some variation in the particular values of ξ and η compared with the hot cluster runs. To see if these quantities correlate with the value of β in these models, we ran a series of cool cluster models in which only the initial temperature was allowed to vary. All other external parameters are the same as those in runs 3 and 4. These are listed as runs 5–10 in Table 1, and the derived values of η and ξ (taken at r_{cool} at $t = 10^{10} \text{ yr}$) are plotted versus β in Figure 10. Other than the

extreme case of $\beta = 0.36$, (which is included only to show that we recover the expected limiting case $\xi, \eta \rightarrow \infty$ as $\beta \rightarrow 0$), the variation with β is slight compared to the dependence of ξ and η on q . In every case the values of ξ and η derived by measuring the time derivatives directly from the models are much closer to the expected values when $q = 1$ than when $q = 4$. We must therefore conclude that the scaling argument of § 2.2 applies only in the limit of small q .

The reason for the inability of equation (4) to predict the flow behavior for large q is not immediately clear, although there are several ways in which the flow may be affected by a large value of q . One is that the rapid mass deposition can significantly reduce the gas density in the interior, thereby reducing the pressure, so that gas slumps to the center from radii well beyond the cooling radius. Unfortunately, there does not appear to be a well-defined position at which to evaluate ξ from observed density and temperature profiles. This is because q is not known in real clusters, and it may be that the relevant cooling radius should be redefined again to account for the high rate of mass deposition in this model. Another possible cause for concern is that if the mass deposition formula (eq. 11) is applied throughout the flow, it implies that matter can condense out even if the local cooling time exceeds the age. To guard against this, we ran models 5–10 with a cutoff to the mass deposition ($q \rightarrow 0$) for $t_{\text{cool}} > t_{\text{age}}$. We also repeated the first four runs with this modification, but there were no differences in the results other than a leveling-off in the dynamical accretion rate at the cooling radius.

3.3. Correspondence to Steady-State Models

We have seen that the dynamical mass accretion rate is a good approximation to the accretion rate one would infer, under the assumption of steady flow, from X-ray observations of the model clusters described above. A further test of the assumption of steady flow is to compute steady-state models corresponding to a fixed time in the evolutionary models. The equations for steady flow are given by WS, and are obtained by setting all partial time derivatives to zero in equations (8)–(10). The resulting ordinary differential equations are then solved numerically subject to appropriate boundary conditions. Because the time-dependent calculation used here and the ODE solver are independent, this is also a further test of the hydrodynamics code.

There are a number of possible ways to specify the three boundary conditions on the steady-state models. Following WS, we choose to fix the age ($t_{\text{age}} = 10^{10}$ yr), and values for the temperature $T|_{r_{\text{cool}}}$ and the dynamical mass accretion rate $\dot{M}|_{r_{\text{cool}}}$ at the cooling radius. For direct comparison with the time-dependent models, we can take the values from Table 1. The solution to the steady flow equations is plotted in Figures 11 (hot cluster) and 12 (cool cluster). These curves can be compared directly to Figures 2 and 4 at $t = 10$ Gyr (solid lines). The agreement is very close, with only a small departure near $r = 0$ in the models with $q = 1$. This difference is not unexpected given the artificial boundary conditions $u|_{r=0} = 0$ imposed in the time-dependent calculations on flows with sonic radii.

4. Time-Dependent Flow in a Static Evolving Potential

One possible limitation to the preceding models is the neglect of cluster evolution. This can consist of dynamical evolution in the form of continued mergers or two-body encounters which act to deepen the cluster potential, or of continued infall of gas from the Hubble flow. The gas itself may contribute to the change in the total potential. M90 included all of these effects in a series of simulations in spherical symmetry. Two classes of models were considered: one with a centrally dominant galaxy (because all cooling flows have one) and one without a central galaxy. We reexamine the effects of cluster evolution on cooling flows and use the same cluster models as M90 so we may compare results. We are interested in whether the flows reach a steady state with or without mass deposition.

4.1. Model Characteristics

In the models of M90, the cluster potential is as described above in equation (14), with an initial velocity dispersion of about 500 km s^{-1} . The depth of the potential is assumed to increase gradually with time until, at the end of each run, the velocity dispersion is about 1000 km s^{-1} . This is done to mock the dynamical evolution of the cluster from a redshift of $z = 1.5$ to $z = 0$, corresponding to a time span running from 3.3 Gyr to 13.1 Gyr (for $\Omega_0 = 1$ and $H_0 = 50 \text{ km s}^{-1} \text{ Mpc}^{-1}$). The gas was assumed to trace the dark matter initially and the central gas temperature put as much energy per unit mass in the gas as in the dark matter. The initial temperature profile was assumed to be adiabatic.

Models without a central galaxy assumed that the initial gas velocity follows the same profile as that for collisionless infall onto a region of overdensity equivalent to that given by the total cluster mass interior to each point. The gas is therefore at rest only at $r = 0$ and at the turnaround radius far outside the cluster, with infall interior to the turnaround radius. Initially the gas in the cluster is thus not in hydrostatic equilibrium, but instead falls inward, then bounces adiabatically. The gas in the center relaxes on a dynamical timescale, which is much less than the cooling time, so the precise initial conditions do not seriously affect the subsequent evolution of the flow. M90 found that gas will cool catastrophically at the center of such flows if $q = 0$, but that for $q = 1/2$ the flow is stabilized against runaway cooling. (Note that M90 employs a different definition of q , and the value of $q = 1/2$ in M90 corresponds to $q = 5/6$ in our notation.)

We are primarily interested in the models of M90 which contain a central galaxy in the initial conditions. In this case, the initial velocity profile is the same as in the case without a central galaxy except that $u = 0$ for $r < 250 \text{ kpc}$, resulting in a discontinuous initial velocity profile.

4.2. Numerical Simulations

Figure 13 shows our simulations using the PLPC code (Lufkin & Hawley 1993) for the fiducial model of M90 with a central galaxy and without mass dropout ($q = 0$). All of the parameters given in M90, including the potential for the central galaxy and the self gravity of the gas, are duplicated here. (We use a different cooling function, which we comment on below.) Up until the second time frame, our results and M90 agree in detail. We note that the discontinuous velocity profile results in an impulsive squeeze on the initially hydrostatic atmosphere interior to r_c . This strong pressure wave travels into the center, bounces off the reflecting inner boundary, and travels back out into the infalling gas beyond r_c . This is evident in both the velocity and temperature profiles at $t = 4$ Gyr (dashed line in Figure 13). We find, using fine time resolution in the data dumps, that two strong bounces occur before the gas relaxes at the center. (The relevant plots in M90 also show evidence for these bounces.) The run begins at $t = 3.3$ Gyr, when the central instantaneous isobaric cooling time is 9.0 Gyr.

For time slices later than 4.0 Gyr, our results differ from those in M90. We find that the gas cools in less than an initial cooling time, with an ensuing cooling catastrophe at the center ($t = 9.9$ Gyr, dot-dash line of Figure 13). For the same model, M90 found no cooling catastrophe.

We have made a number of tests to search of the source of this discrepancy with the results of M90. First, the calculations were repeated using exactly the same grid of 150 zones as used in M90:

$$\begin{aligned} r_i &= 1.88 \text{ kpc}(i - 1) & i \leq 21 \\ r_i &= 1.046r_{i-1} & i > 21. \end{aligned}$$

For comparison, we also made plots which were 1-2-1 smoothed (as in M90), but detected no variation from those shown in Figure 13. Second, we considered the effects of differences in the cooling function in the two sets of models. The cooling function adopted in M90 is that of Gaetz & Salpeter (1983), whereas we have used that of WS, which is somewhat stronger. We therefore ran the case with a central galaxy with the strength of the cooling function reduced by 20% to compensate. The result was virtually unchanged. This is not surprising, since the cooling rate is proportional to the square of the density. It therefore appears unlikely that the disparate results are caused by small differences in the cooling functions. Finally, we have run the fiducial model with two other hydro codes, the direct-Eulerian MONO scheme of Hawley, Smarr, & Wilson (1984) and a modified version of the implicit scheme of Ruppell & Cloutman (1975). Although the exact time of cooling collapse varies by about 20% (this measure is very sensitive to the value of the central density, which in turn is sensitive to the numerical diffusion as the impulsive compression waves bounce off the center early in the simulation), the density, velocity and temperature profiles agree in detail with the calculation of Figure 13.

One possible reason for this discrepancy is the grid noise (zone-to-zone variations in the fluid variables) present in the numerical calculations of M90. This could cause sound waves to be

amplified or converted into heat energy, perhaps via artificial viscosity. We also note that the crests in the temperature and velocity profiles are sharper in our calculation than in the figures of M90. This is true even when our model output is smoothed identically to that present in M90. This suggests that the features in the plots in M90 are spread over several grid zones, which might indicate that a significant level of numerical diffusion was present. Such diffusion may have transported heat energy into the core.

We find that a cooling catastrophe occurs either with or without the central galaxy. We do reproduce the result in M90 that the catastrophe occurs sooner in the case without a central galaxy even though the initial cooling time is longer. As suggested in M90, this is likely due to the homologous collapse of the constant-density core.

When mass deposition is included, the flow reaches a steady state on an initial cooling timescale. The details in the flow variables appear to be affected by transient features left over from the discontinuous initial conditions ($q = 1$ and 4 ; Figures 14–17). In particular, there are discontinuities in the position of the cooling radius due to the shock waves that bounced off the center at the beginning of the runs. As expected, the temperature beyond 100 kpc increases gradually due to continued shock heating from secondary infall.

The agreement between the cooling and dynamical accretion rates is also quite close, as in the static models of § 3. Thus, we conclude that flows with mass deposition do reach a steady state when cluster evolution and secondary infall are included in the spherical model. For both runs, \dot{M} stays constant to within a factor of two after the flows reach a steady state. Evolutionary effects in spherical symmetry therefore do not appear to affect the time evolution of the mass accretion rate relative to that found for static clusters.

5. Discussion and Conclusions

We have solved for the time-dependent behavior of cooling gas in a variety of spherically symmetric cluster models, with particular emphasis on the evolution of the mass accretion rate.

We find that the steady-state approximation is valid after the initial onset of cooling at the center for cluster flows in both static and evolving external potentials. This result is insensitive to the inclusion of self-gravity. For the models considered here the accretion rate either increases or stays about the same with time. While the rates of increase or decrease that we see in the simulations would be difficult to infer from imaging observations, spatially resolved spectra can be a useful diagnostic (e.g., Wise & Sarazin 1993). The difference arises from the fact that while the age is an assumed parameter in the models, it can be *measured* by calculating the cooling time at the radius of extent of soft X-ray lines. Moreover, the cooling rates derived from imaging are more model-dependent, than those derived from spectra, which can in principle be obtained from a measure of the mass cooling through a single line.

A decreasing accretion rate with time is seen only for cases where the temperature of the gas corresponds closely to the cluster velocity dispersion ($\beta = 1$). In a number of clusters, especially poorer ones, the gas may be hotter by a factor of two than the virial temperature measured from galaxy motions. Thus, although we cannot rule out a decreasing mass accretion rate on the basis of these experiments, nearly constant or increasing accretion rates are favored for most clusters, unless they have been strongly affected by mergers. In the absence of mergers, the spherical model with mass deposition would predict that cooling flows were not much more vigorous in the recent past than they are today. Attempts to include additional evolutionary effects via secular deepening of the cluster potential well and continued accretion from the Hubble flow in spherical symmetry do not alter these results. However, it is likely that cluster mergers can have a strong effect on cooling flows (e.g., McGlynn & Fabian 1984; Gómez et al. 2000). Further study of the effect of cluster evolution on cooling flows will require numerical simulations in three dimensions with high spatial resolution and including cooling.

We would like to thank Steve Balbus, Joel Bregman, John Hawley, Brian McNamara, Avery Meiksin, Bill Sparks and Mike Wise for numerous informative discussions. E. A. L. acknowledges the support of NSF grants PHY90-18251 and AST-8919180. C. L. S. was supported in part by NASA Astrophysical Theory Program grant NAGW-2376. R. E. W. III was supported in part by the NSF and the State of Alabama through EPSCoR II and by a National Research Council Senior Research Associateship at NASA GSFC.

REFERENCES

- Allen, S. W., Fabian, A. C., Johnstone, R. M., Arnaud, K. A., & Nulsen, P. E. J. 2000, MNRAS, in press (astro-ph/9910188)
- Bailey, M. E., & MacDonald, J. 1981, MNRAS, 194, 195
- Bertschinger, E. 1988, in *Cooling Flows in Clusters and Galaxies*, ed. A. C. Fabian, (Dordrecht: Kluwer), 337
- Bertschinger, E. 1989, ApJ, 340, 666
- Binney, J., & Tremaine, S. 1987, *Galactic Dynamics*, (Princeton: Princeton University Press)
- Bird, C. M. 1994, AJ, 107, 1637
- Bregman, J. N., & David, L. P. 1988, ApJ, 326, 639
- Bregman, J. N., & David, L. P. 1989, ApJ, 341, 49
- Canizares, C. R., Markert T. H., & Donahue M. E. 1988, in *Cooling Flows in Clusters and Galaxies*, ed. A. C. Fabian (Dordrecht: Kluwer), 63
- Chevalier, R. A. 1987, ApJ, 318, 66
- Chevalier, R. A. 1988, ApJ, 329, 16
- Evrard, A. E. 1990, ApJ, 363, 349
- Fabian, A. C. 1994, ARA&A, 32, 277
- Gaetz, T., & Salpeter E. 1983, ApJS, 52, 155
- Gómez, P. L., Loken, C., Burns, J. O., & Roettinger, K. 2000, preprint
- Hawley, J. F., Smarr, L. L., & Wilson J. R. 1984, ApJS, 55, 211
- Jones, C., & Forman, W. 1984, ApJ, 276, 38
- Lufkin, E. A., Balbus, S. A., & Hawley, J. F. 1995, ApJ, 446, 529
- Lufkin, E. A., & Hawley, J. F. 1993, ApJS, 88, 569
- Markevitch, M., Forman, W. R., Sarazin, C. L., & Vikhlinin, A. 1998, ApJ, 503, 77
- McGlynn, T. A., & Fabian, A. C. 1984, MNRAS, 208, 709
- Meiksin, A. 1988, ApJ, 334, 59
- Meiksin, A. 1990, ApJ, 352, 466 (M90)
- Navarro, J. F., Frenk, C. S., & White, S. D. M. 1997, ApJ, 490, 493
- Peres, C. B., Fabian, A. C., Edge, A. C., Allen, S. W., Johnstone, R. M., & White, D. A. 1998, MNRAS, 298, 416
- Raymond, J. C., Cox, D. P., & Smith, B. W. 1976, ApJ, 204, 290
- Ruppell, H. M., & Cloutman, L. D. 1975, Los Alamos Nat. Lab. Rept. LA 6149-MS

- Sarazin, C. L., & Graney, C. M. 1991, *ApJ*, 375, 552
- Stewart, G. C., Canizares, C. R., Fabian, A. C., & Nulsen, P. E. J. 1984, *ApJ*, 278, 536
- Thomas, P. A., Fabian, A. C., & Nulsen, P. E. J. 1987, *MNRAS*, 228, 973
- White, D. A. 2000, *MNRAS*, in press (astro-ph/9909467)
- White, D. A., Jones, C., & Forman, W. 1997, *MNRAS*, 292, 419
- White, R. E. III 1991, *ApJ*, 367, 69
- White, R. E. III 1988, in *Cooling Flows in Clusters and Galaxies*, ed. A. C. Fabian, (Dordrecht: Kluwer), 343
- White, R. E. III, & Sarazin, C. L. 1987, *ApJ*, 318, 629 (WS)
- Wise, M. W. & Sarazin, C. L. 1993, *ApJ*, 415, 58

Fig. 1.— Plot of gravitational acceleration g versus radius for four model galaxies. The dotted line is a King approximation to an isothermal sphere ($\rho \sim r^{-3/2}$ at large r). The short-dashed line corresponds to the same distribution truncated at 20 core radii. The long-dashed line gives the acceleration due to the superposition of two Plummer’s models (derived from equation 16), with the parameters as stated in the text. The solid line is for a true King model with the central potential equal to $7\sigma_c^2$.

Fig. 2.— The fully time-dependent solution for the hot cluster $q = 1$ model (run 1 in Table 1). The four panels show total number density, temperature, dynamical mass accretion rate, and instantaneous isobaric cooling time as functions of radius shown at $t = 0$ (dotted line), 3 (short dash), 6 (long dash), 10 (solid) and 15 Gyr (dot-dash).

Fig. 3.— Comparison of accretion rates for the $q = 1$ model of Figure 2. The top left panel shows the time evolution of the cooling radius determined from the instantaneous isobaric cooling time (eq. 1, solid line) and the integrated isobaric cooling time (eq. 3; dotted line). The upper right and lower left panels show the dynamical mass accretion rate $\dot{M} = -4\pi r^2 \rho u$ and the cooling mass accretion rate derived from the X-ray emission \dot{M}_X , respectively. The solid (dotted) curve corresponds to taking the accretion rate at the radius where the instantaneous (integrated) cooling time equals the age. The panel at lower right gives the estimated logarithmic time derivative of the mass accretion rate as a function of cooling radius (eq. 4) at the end of the run.

Fig. 4.— The time-dependent solution for the hot cluster $q = 4$ model (run 2 in Table 1). The notation is the same as Figure 2.

Fig. 5.— Same as Figure 3, but for the hot cluster $q = 4$ model (run 2 in Table 1).

Fig. 6.— Cool cluster model with $q = 1$ (run 3 in Table 1). The notation is the same as in Figure 2.

Fig. 7.— Cool cluster model with $q = 1$ (run 3 in Table 1). The notation is the same as in Figure 3.

Fig. 8.— Cool cluster model with $q = 4$ (run 4 in Table 1). The notation is the same as in Figure 2.

Fig. 9.— Cool cluster model with $q = 4$ (run 4 in Table 1). The notation is the same as in Figure 3.

Fig. 10.— Top panel: the logarithmic rate of change of the cooling radius with time as a function of β for flows in a static potential. Bottom panel: the logarithmic rate of change of the dynamical mass accretion rate with time as a function of β . Filled figures correspond to models with $q = 4$ and open figures to $q = 1$; The triangles represent values that one would estimate by applying equation (4) to ideal observations of the model clusters, while the squares are the values obtained by direct measurement from the simulations. Here, the failure of equation (4) results from two

separate causes. In the $q = 1$ models the cooling flows are too young for complete cooling in the center, and in the $q = 4$ models the strong mass deposition results in structural changes that reach far beyond the fiducial cooling radius. Because the value of q in real clusters is not known, we must conclude that it is very difficult to measure reliably the rate of change of \dot{M} directly from X-ray images.

Fig. 11.— Steady-state cooling flow solutions for the hot cluster runs in Figures 2 and 4 obtained using the method of White & Sarazin (1987). The four panels show total number density, temperature, mass accretion rate and instantaneous isobaric cooling time as functions of radius for $q = 1$ and $q = 4$.

Fig. 12.— Same as Figure 11 except for the cool cluster runs of Figures 6 and 8.

Fig. 13.— Our simulation of the fiducial run of M90 with a central galaxy and $q = 0$. The evolution times are 3.3 Gyr (initial conditions; dotted line), 4.0 (short dash), 7.0 (long dash) and 9.9 Gyr (dot-dash). A cold core has developed in the innermost grid zone by 9.9 Gyr, preventing continued numerical evolution.

Fig. 14.— Same as Figure 13 but for $q = 1$. The dot-dashed and solid lines correspond here to $t = 10.0$ and 13.0 Gyr.

Fig. 15.— The evolution of cooling radius parameters in our simulation of the the $q = 1$ M90 model (same notation as Figure 3). The structure in the time-dependence of the mass accretion rate is due to transient sound waves and shocks resulting from non-static initial conditions. Despite these effects, the dynamical and cooling accretion rates trace each other quite well, indicating that the flow has reached a steady state.

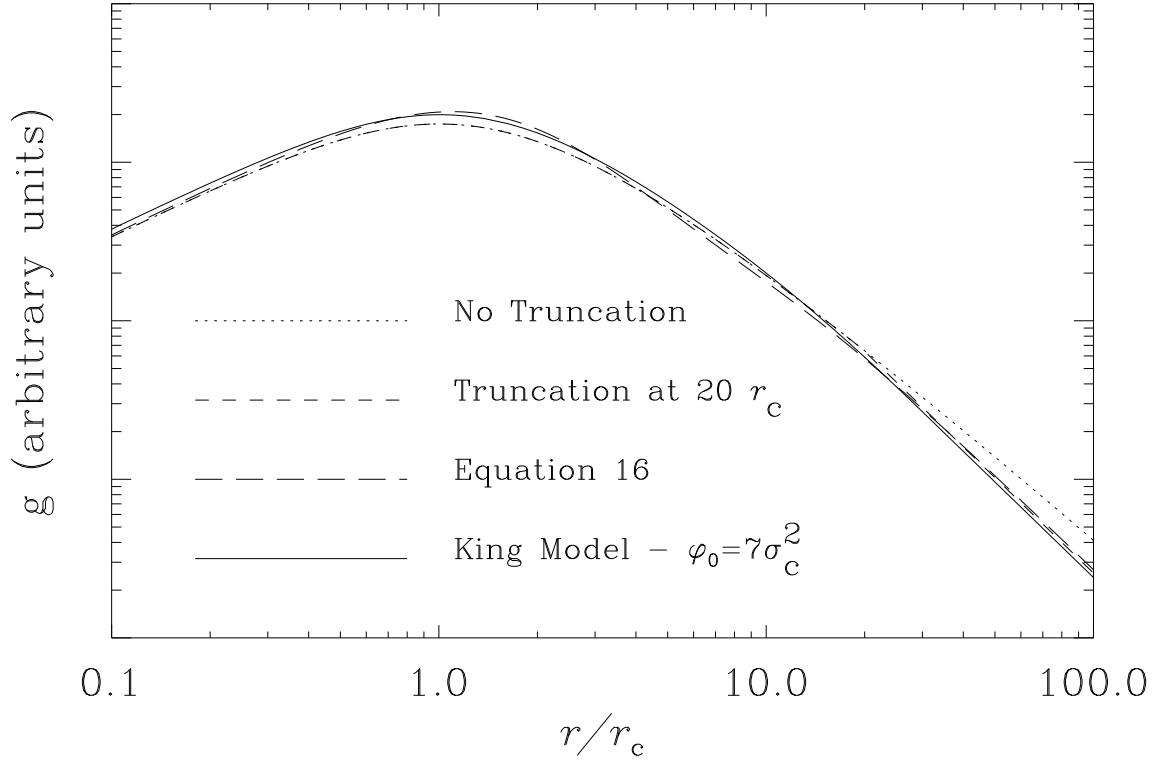
Fig. 16.— Same as Figure 14 but for $q = 4$.

Fig. 17.— Same as Figure 16 but for $q = 4$.

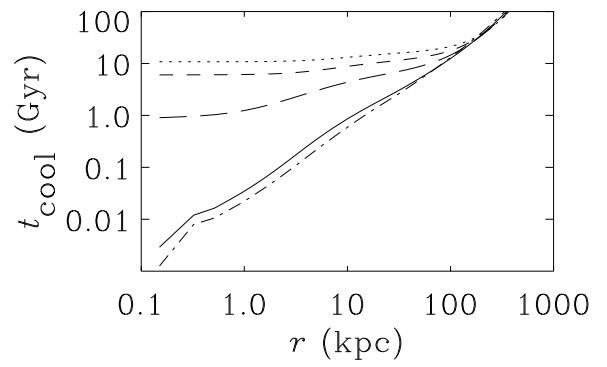
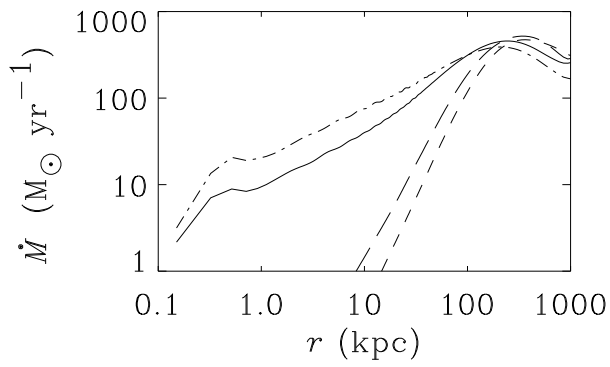
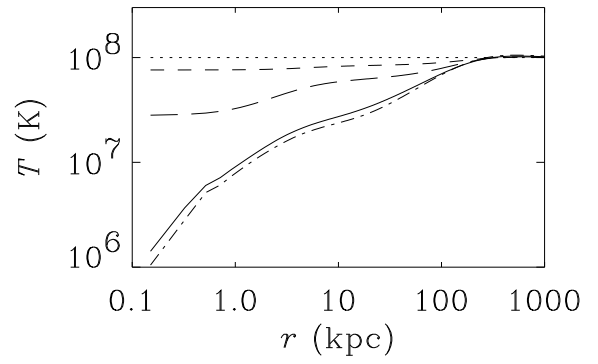
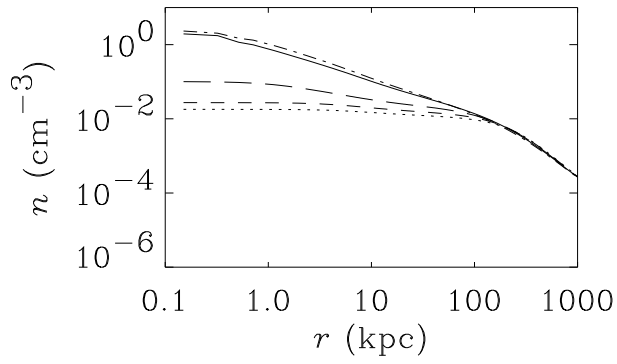
Table 1: Model Parameters

Run	σ_c (km s^{-1})	q	T_∞ (10^7 K)	β	n_0^a (cm^{-3})	$t_{\text{cool},0}^a$ (Gyr)	r_{cool} (kpc)	$\dot{M} _{r_{\text{cool}}}$ ($M_\odot \text{ yr}^{-1}$)	$T _{r_{\text{cool}}}$ (10^7 K)
1	1054	1	10.0	0.83	1.8	10.8	86	278	6.5
2	1054	4	10.0	0.83	3.3	5.9	69	244	7.6
3	527	1	3.0	0.69	1.8	5.2	68	65	2.1
4	527	4	3.0	0.69	3.3	2.8	60	93	2.4
5	527	1	1.5	1.38	1.8	2.0	23	1.4	1.2
6	527	4	1.5	1.38	3.3	1.1	23	2.7	1.3
7	527	1	2.0	1.04	1.8	3.0	45	10	1.5
8	527	4	2.0	1.04	3.3	1.6	39	15	1.6
9	527	1	5.0	0.42	1.3	10.0	64	53	3.3
10	527	4	5.0	0.42	1.3	10.0	34	18	3.3

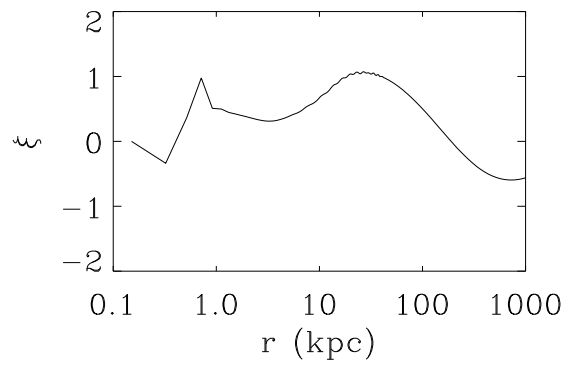
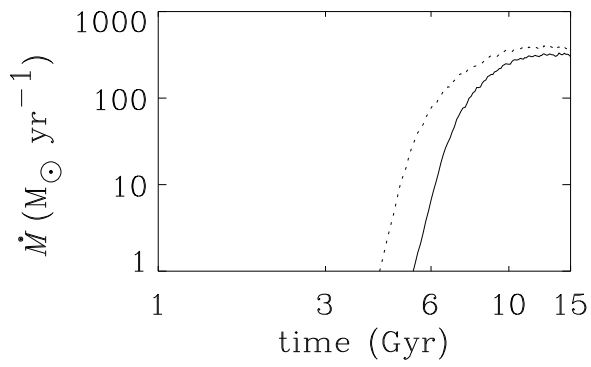
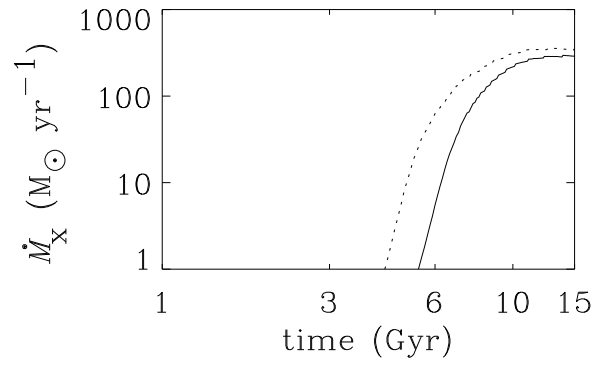
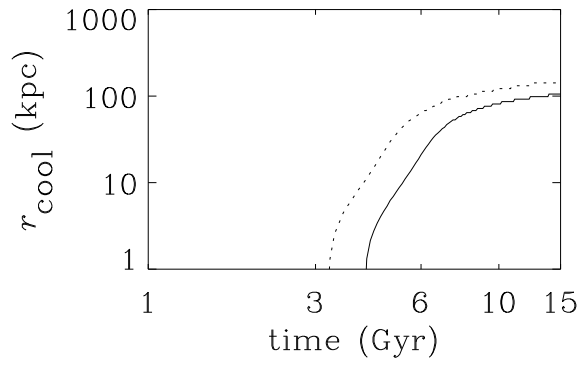
^aValues with a subscript of 0 refer to initial central values at a radius $r = 0$.



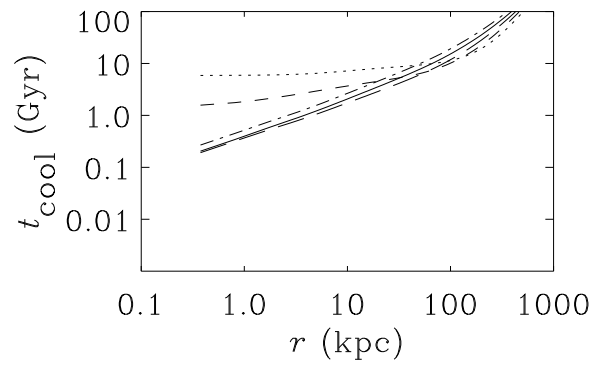
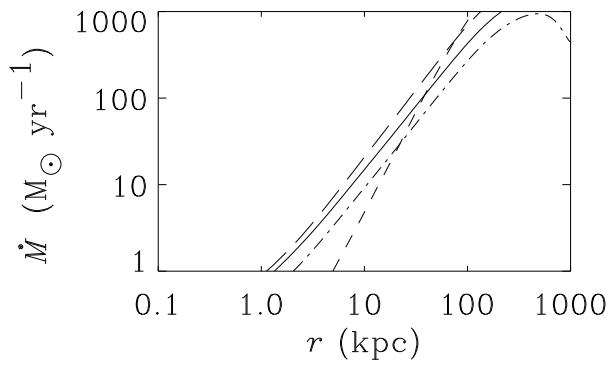
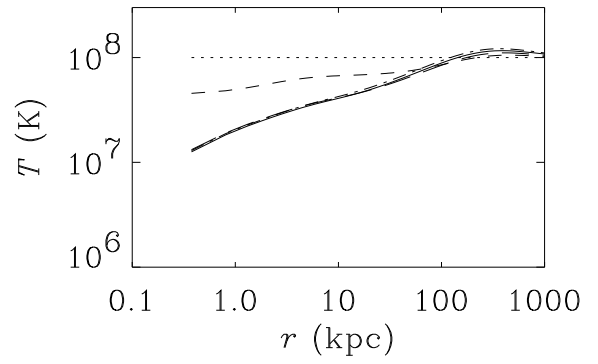
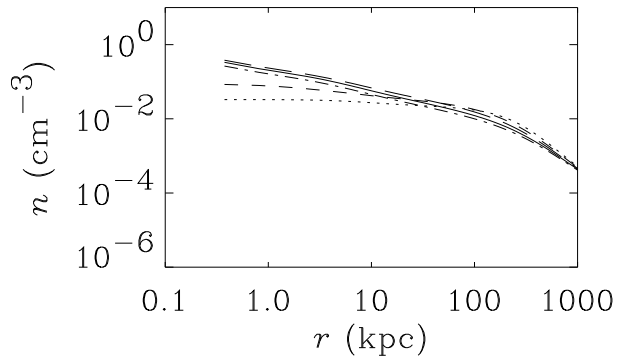
Hot cluster — $q = 1$



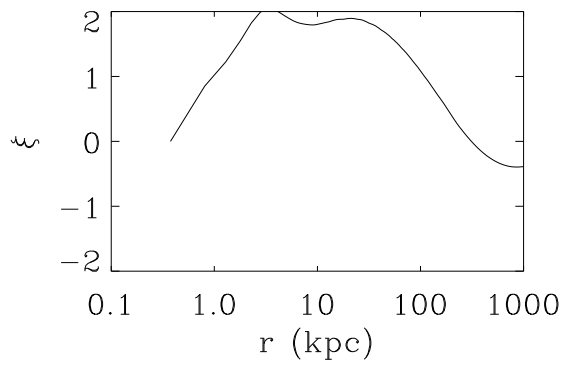
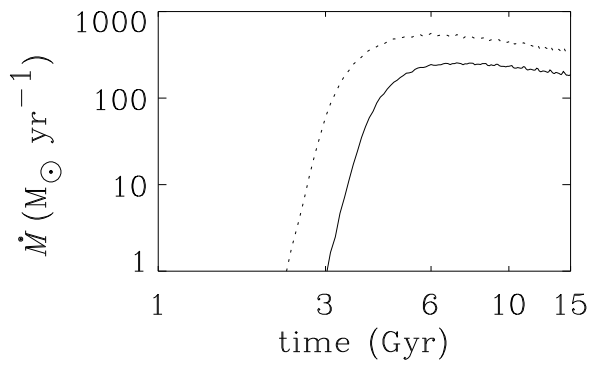
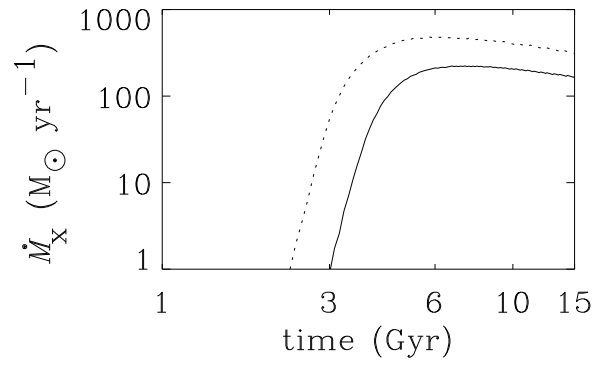
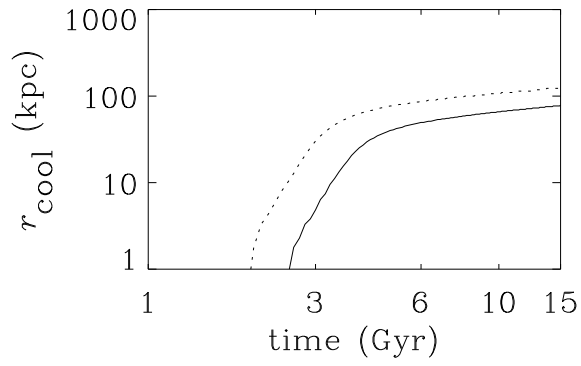
Hot cluster — $q = 1$



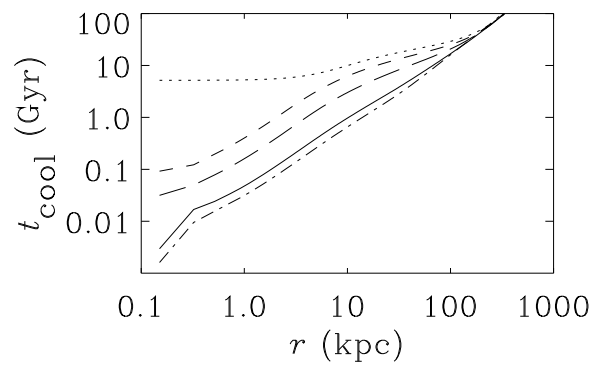
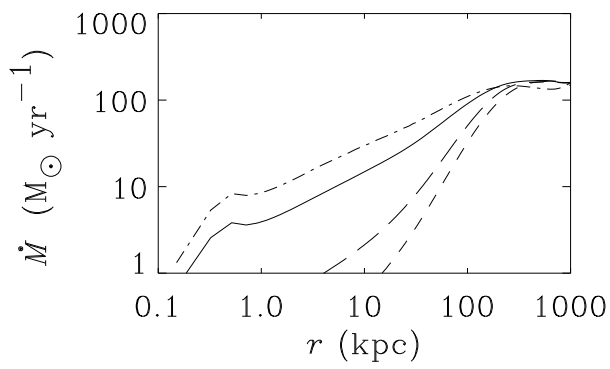
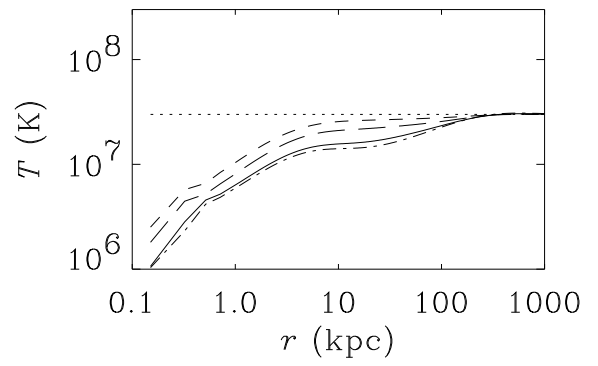
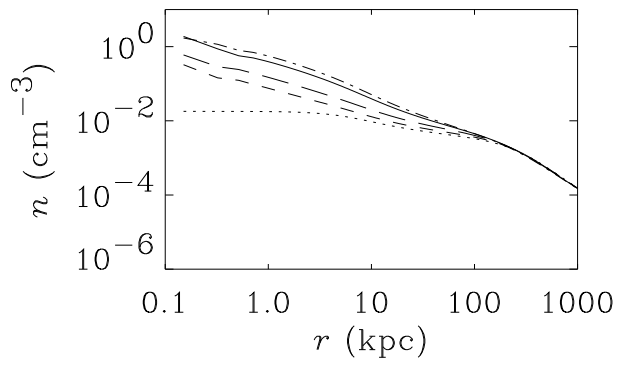
Hot cluster — $q = 4$



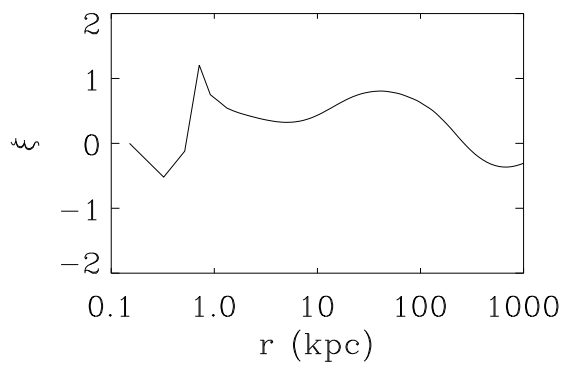
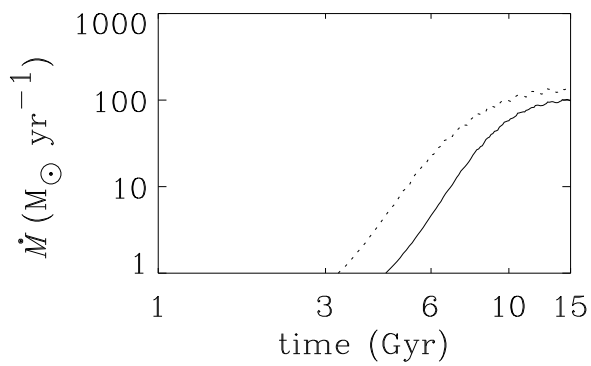
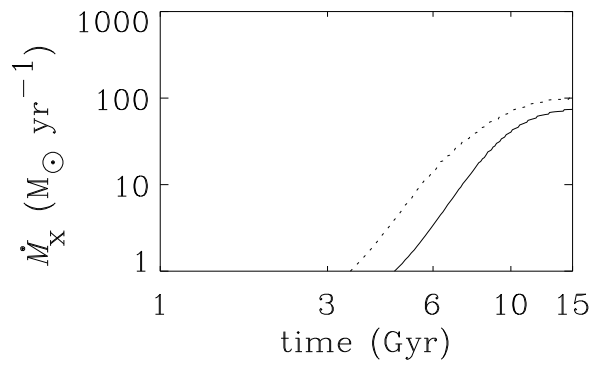
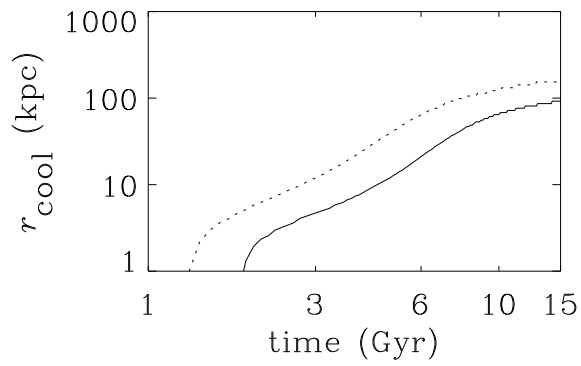
Hot cluster — $q = 4$



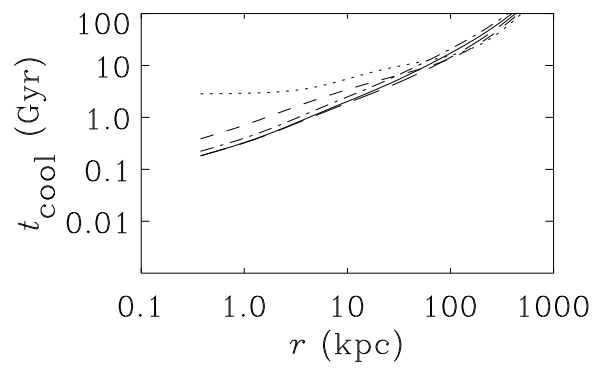
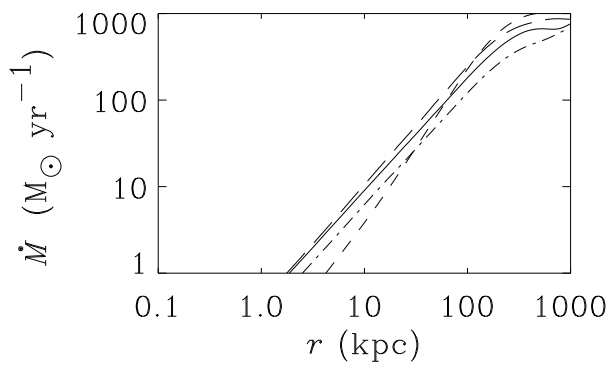
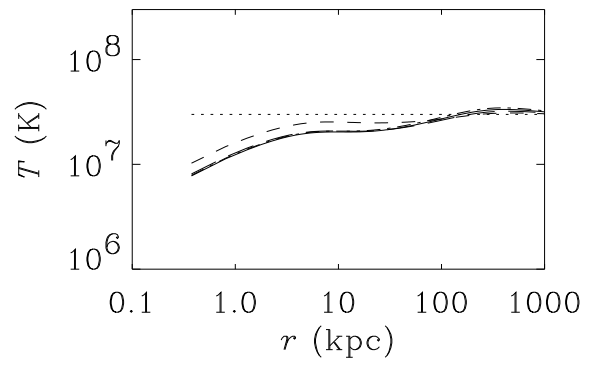
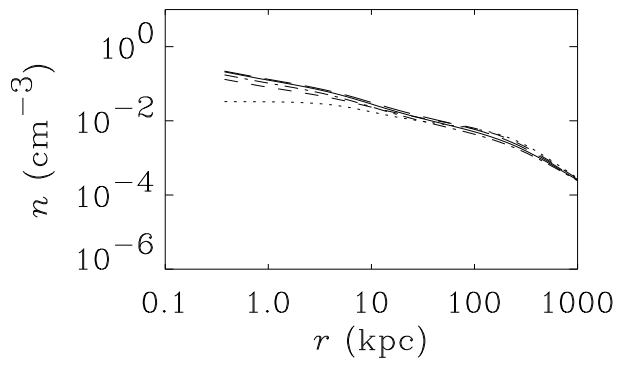
Cool cluster — $q = 1$



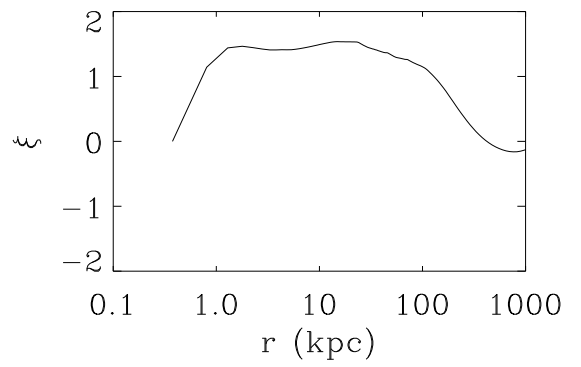
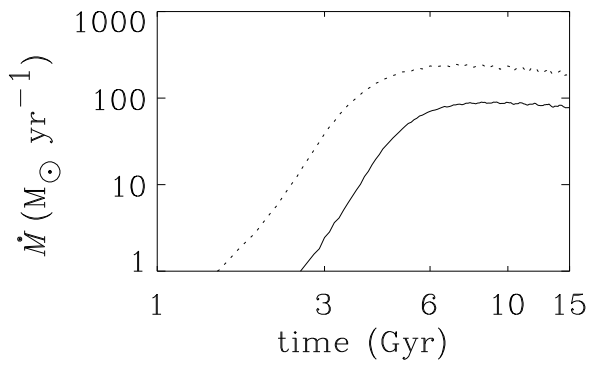
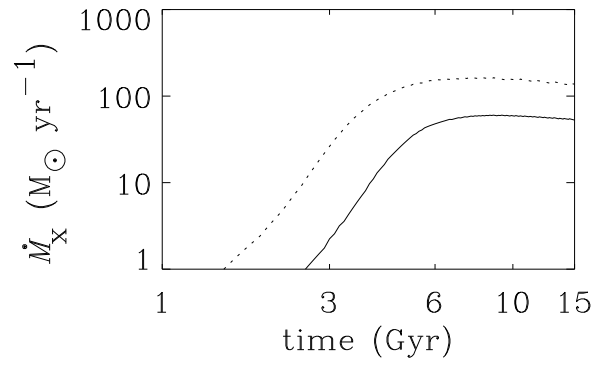
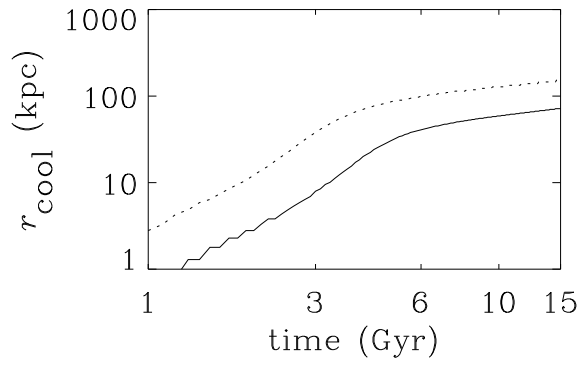
Cool cluster — $q = 1$

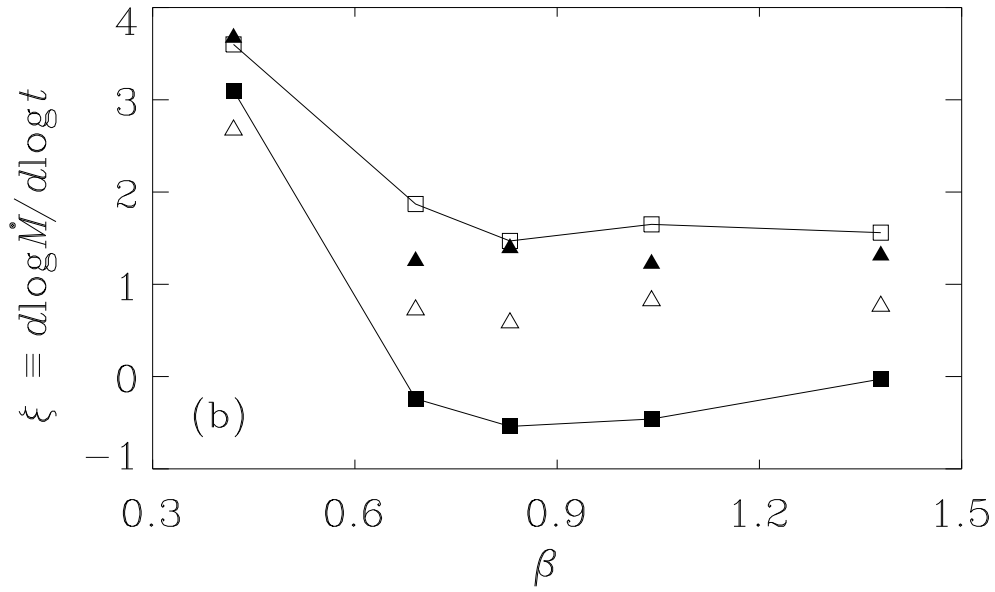
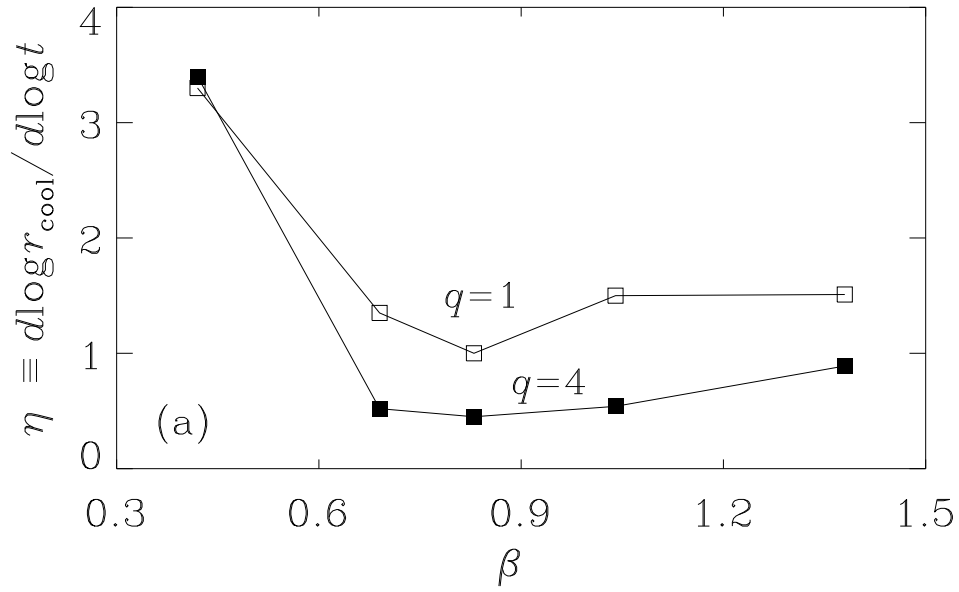


Cool cluster — $q = 4$

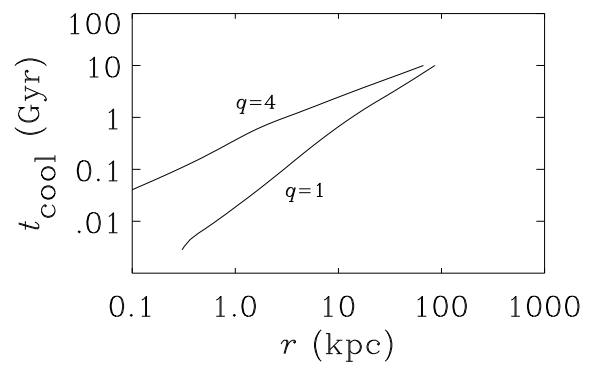
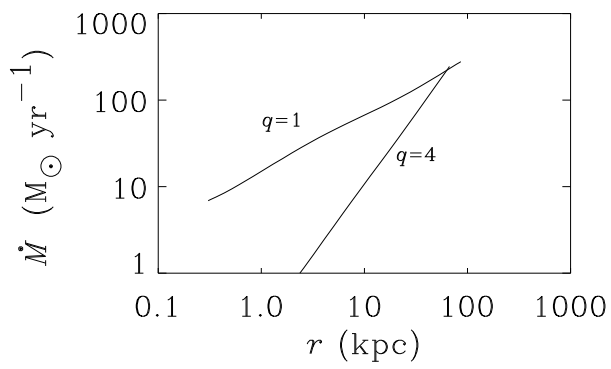
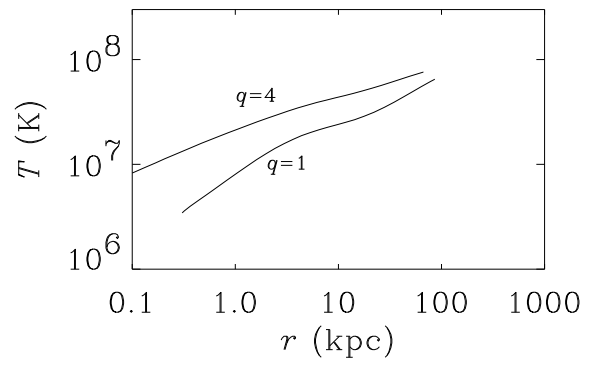
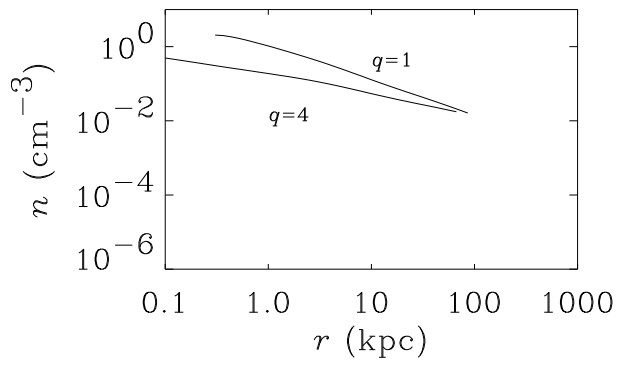


Cool cluster — $q = 4$

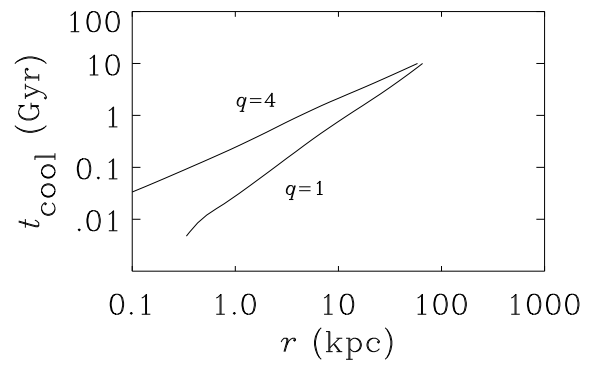
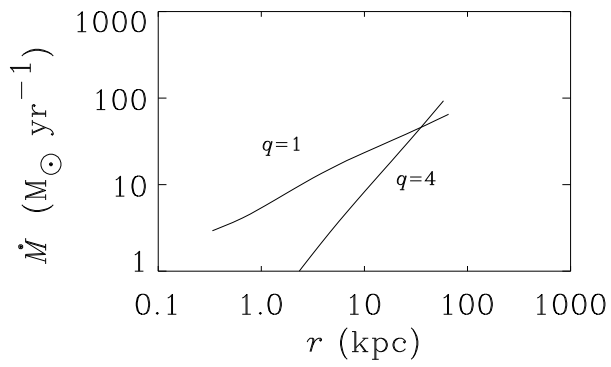
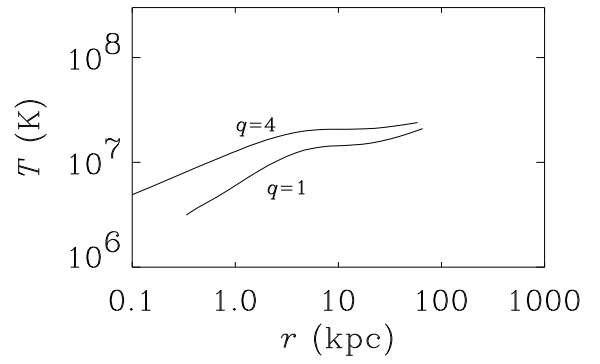
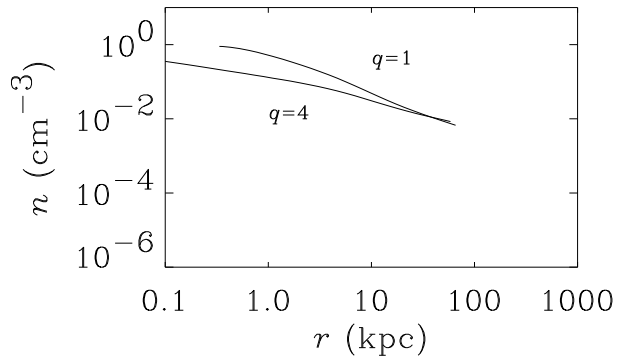




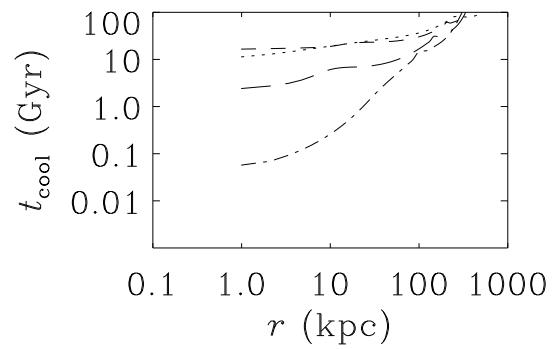
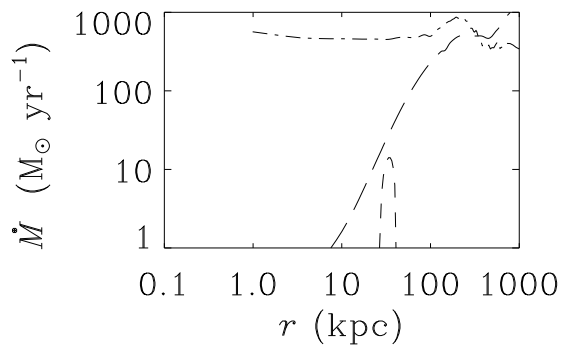
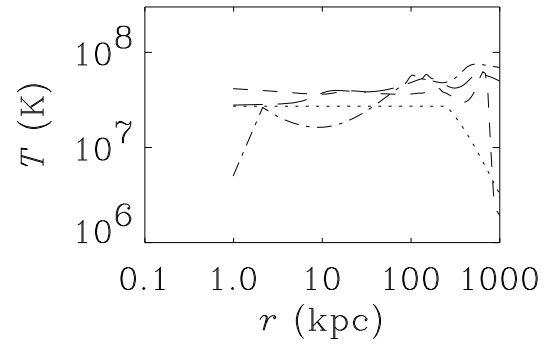
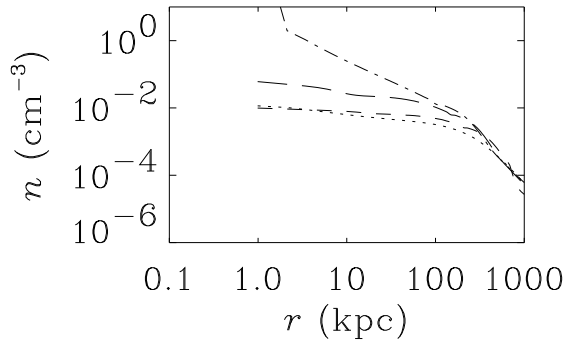
Hot cluster



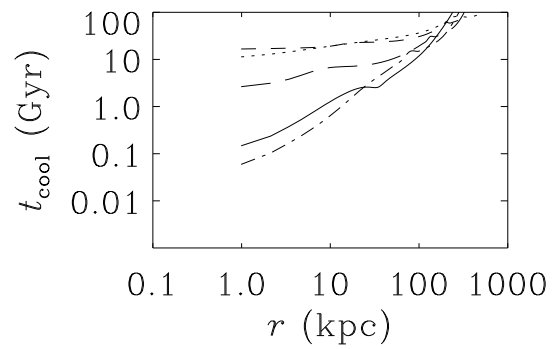
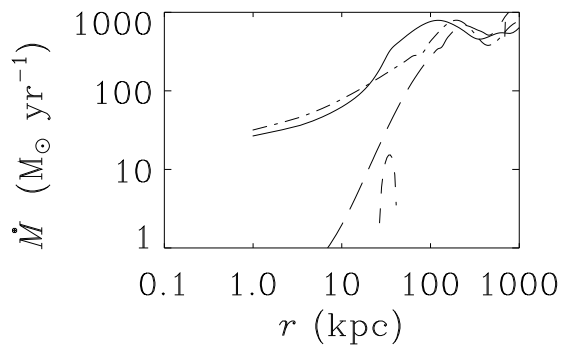
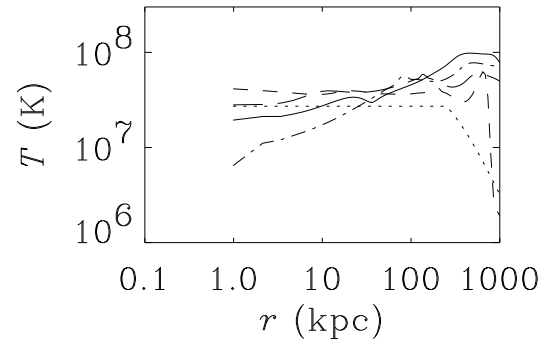
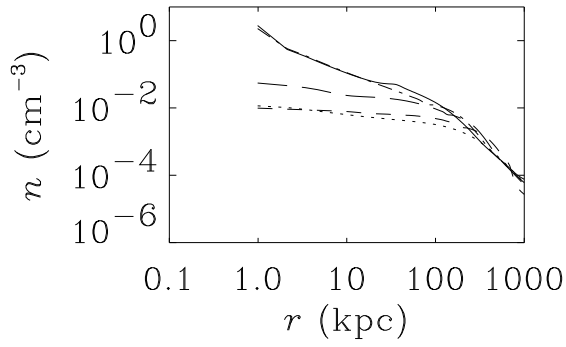
Cool cluster



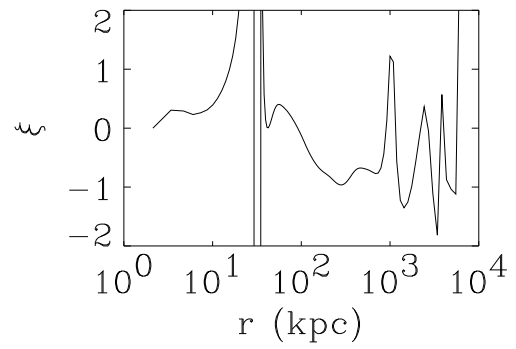
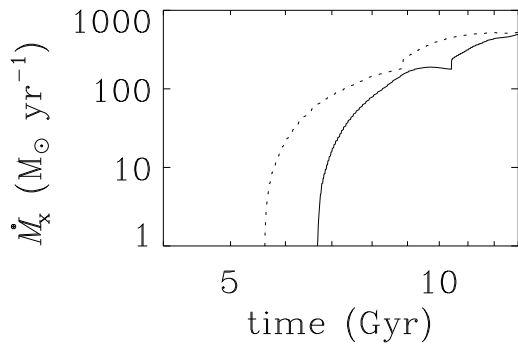
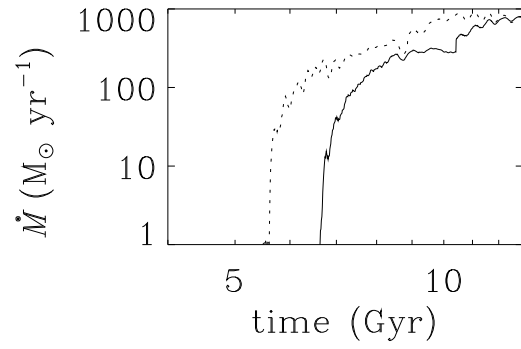
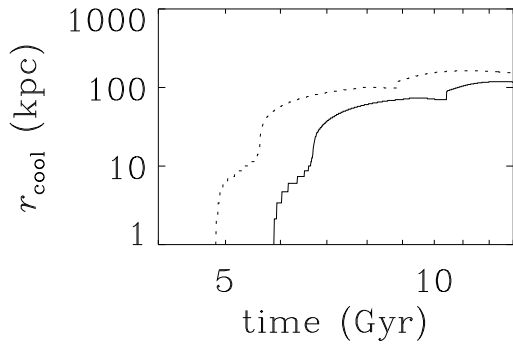
M90 simulation — $q = 0$



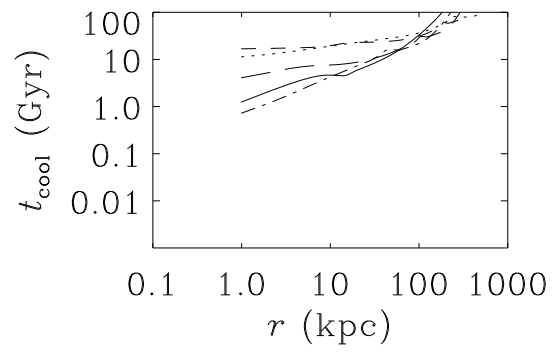
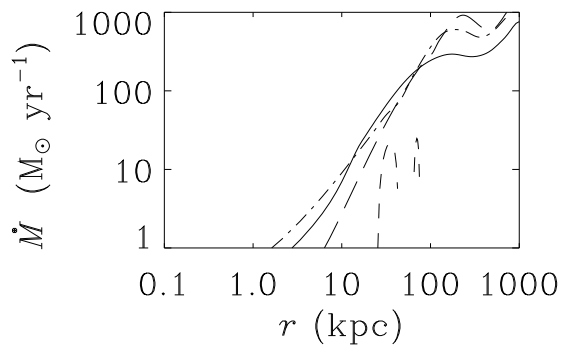
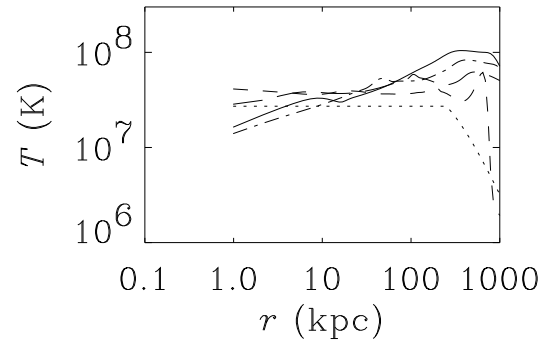
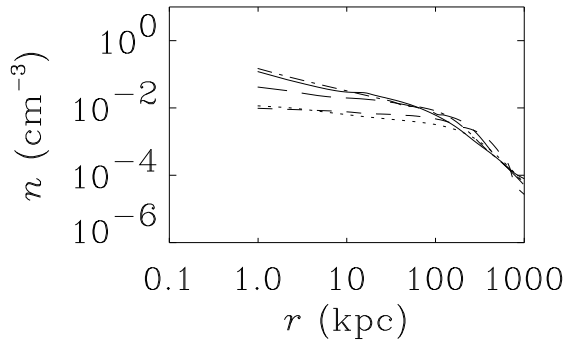
M90 simulation — $q = 1$



M90 simulation — $q = 1$



M90 simulation — $q = 4$



M90 simulation — $q = 4$

